arXiv:1408.2598v2 [astro-ph.SR] 13 Jan 2016

Simulations of the Kelvin-Helmholtz instability driven by coronal mass ejections in the turbulent corona

Daniel O. Gómez[1] and Edward E. DeLuca

Harvard-Smithsonian Center for Astrophysics, 60 Garden St, Cambridge, MA 02138

and

Pablo D. Mininni

Departamento de Física, Facultad de Ciencias Exactas y Naturales, Universidad de Buenos Aires & Instituto de Física de Buenos Aires, Ciudad Universitaria, 1428 Buenos Aires, Argentina.

Received _____; accepted _____

To appear in Astrophys. J.

[1]On sabbatical leave from Departamento de Física, Facultad de Ciencias Exactas y Naturales, Universidad de Buenos Aires & Instituto de Astronomía y Física del Espacio, Ciudad Universitaria, 1428 Buenos Aires, Argentina.

ABSTRACT

Recent high resolution AIA/SDO images show evidence of the development of the Kelvin-Helmholtz instability, as coronal mass ejections (CMEs) expand in the ambient corona. A large-scale magnetic field mostly tangential to the interface is inferred, both on the CME and on the background sides. However, the magnetic field component along the shear flow is not strong enough to quench the instability. There is also observational evidence that the ambient corona is in a turbulent regime, and therefore the criteria for the development of the instability are a-priori expected to differ from the laminar case.

To study the evolution of the Kelvin-Helmholtz instability with a turbulent background, we perform three-dimensional simulations of the incompressible magnetohydrodynamic equations. The instability is driven by a velocity profile tangential to the CME-corona interface, which we simulate through a hyperbolic tangent profile. The turbulent background is generated by the application of a stationary stirring force. We compute the instability growth-rate for different values of the turbulence intensity, and find that the role of turbulence is to attenuate the growth. The fact that the Kelvin-Helmholtz instability is observed, sets an upper limit to the correlation length of the coronal background turbulence.

Subject headings: instabilities, magnetohydrodynamics, Sun: coronal mass ejections, turbulence

1. Introduction

Shear flows are ubiquitous in astrophysical problems, such as jet propagation in the interstellar medium (Ferrari, Trussoni & Zaninetti 1980; Begelman, Blandford & Rees 1984; Bodo et al. 1994), the dynamics of spiral arms in galaxies (Dwarkadas & Balbus 1996), cometary tails (Ershkovich, Nusinov & Chernikov 1973; Brandt & Mendis 1979) and differential rotation in accretion disks (Balbus & Hawley 1998). It is also relevant in a variety of space physics problems, such as zonal flows in the atmospheres of rotating planets like Jupiter (Hasegawa 1985), the solar wind (Poedts, Rogava & Mahajan 1998) or the Earth's magnetopause (Parker 1958).

Shear flows often give rise to the well-known Kelvin-Helmholtz (KH) instability (Helmholtz 1868; Kelvin 1871), which has been extensively studied by Chandrasekhar (1961). It is an ideal hydrodynamic instability, that converts the energy of the large-scale velocity gradients into kinetic and/or magnetic energy at much smaller scales. The presence of a magnetic field component parallel to the shear flow has a stabilizing effect, and can even stall the instability if the parallel component of the Alfven velocity becomes larger than one half of the shear velocity jump (Lau & Liu 1980; Miura & Pritchett 1982). A similar instability condition was anticipated by Ershkovich, Nusinov & Chernikov (1973) in connection with observational evidence of KH in comet tails. On the other hand, an external magnetic field pointing in any direction perpendicular to the shear flow has no effect on the linear regime of the instability, and it is simply advected by the flow.

The first observations of a KH pattern in the solar corona were reported by Foullon et al. (2011) for a 2010 November 3 event using data from the Atmospheric Imaging Assembly (AIA) on board the *Solar Dynamics Observatory* (SDO). Ofman & Thompson (2011) also reported observations of a KH pattern obtained by AIA/SDO for an 2010 April 8 event. AIA produces high spatial resolution (pixel size of 0.6 arcsec) and high temporal

cadence (10-20 sec) images of the Sun in several bandpasses covering white light, ultraviolet and extreme ultraviolet. The observed pattern of the Kelvin-Helmholtz instability observed by Foullon et al. (2011) extends from about 70 Mm up to about 180 Mm above the solar surface (1 $Mm = 10^3$ km). When a coronal mass ejection (CME) expands supersonically upwards from the solar surface, a bow shock is formed ahead of the CME and a strong shear flow develops across the contact discontinuity separating the shocked ambient plasma from the ejected material. A similar configuration arises at the flanks of the Earth magnetopause, where the KH instability has also been observed and studied (Fujimoto & Teresawa 1995; Fairfield et al. 2000; Nykyri & Otto 2001). More recently it was observed in connection to the magnetopause of other planets, such as Saturn (Masters et al. 2010) and Mercury (Sundberg et al. 2011). When the supersonic solar wind impinges on these magnetized planets, it first crosses a bow shock (and becomes subsonic in the reference frame of the planet) and then circumvents the planet slipping through the outer part of a surface of tangential discontinuity known as the *magnetopause*, where a strong shear flow is generated.

The ambient corona is expected to be turbulent, as evidenced by measurements of non-thermal broadenings of highly ionized spectral lines. Most recent observations of nonthermal broadenings obtained by the Extreme-ultraviolet Imaging Spectrometer (EIS) on board *Hinode*, correspond to nonthermal motions in the range of $20 - 60$ $km.s^{-1}$ (Doschek et al. 2014). The typical sizes of these nonthermal motions are sufficiently small to remain unresolved by EIS, whose pixel size is 2 *arcsec*, and therefore its only manifestation is an excess in the Doppler broadening of spectral lines (i.e. beyond the thermal Doppler broadening).

The goal of the present paper is to study the interaction between these two rather dissimilar features: the large-scale laminar pattern generated by the ongoing KH instability, and the small-scale nonthermal motions presumably corresponding to a well developed

turbulence. With this goal in mind, we set up three-dimensional simulations of the MHD equations, to study the evolution of the KH instability in the presence of a turbulent ambient background. Nykyri & Foullon (2013) presented results from a large number of compressible 2.5D MHD simulations (without a turbulent background) for parameter values compatible with the observations of the 2010 November 3 event. This comparison is consistent with a magnetic field almost perpendicular to the flow plane, and therefore we make this assumption in our simulations. When a small-scale turbulent background is considered, the expected role on a large-scale flow is to produce the effect of an enhanced diffusivity which can be characterized through an effective or turbulent viscosity. The effect of this extra diffusivity on an ongoing instability for the large-scale flow, as it is currently the case for KH, is to reduce its growth rate or even to switch-off the instability completely. We test and basically confirm this theoretical picture with a series of simulations of a KH-unstable shear flow superimposed on a small-scale turbulent background with different turbulence intensities. The AIA observations showing a KH pattern are described in § 2.1 and the observed features of small-scale turbulence are summarized in § 2.2. We introduce the MHD equations in § 3 and describe the basic properties of the Kelvin-Helmholtz instability in §4. The characteristic features of the turbulent background generated in our simulations are discussed in § 5 and our numerical results are shown in § 6. The potential consequences of the results presented in this paper are discussed in §7, and our conclusions are listed in § 8.

2. Observations

2.1. AIA observations

The coronal mass ejection (CME) that occurred on 2010 November 3 near the southeast solar limb, showed the characteristic pattern of the KH instability on AIA images. This

pattern has only been observed at the highest temperature channel, centered at the 131$\mathring{A}$ bandpass at 1.1 10^7 K. The sequence of AIA images shows a regular array of three to four vortex-like structures on the northern flank of the CME, that were interpreted by Foullon et al. (2011) as the manifestation of an ongoing KH instability. The geometrical setup of a CME expanding upwards from the solar surface is similar to the one taking place at the Earth's magnetopause (Foullon et al. 2011). In view of this similarity, these authors termed *CME-pause* to the surface of tangential discontinuity that separates the plasma of the ejecta from the shocked plasma of the ambient corona.

From these observations, Foullon et al. (2013) were able to estimate several of the relevant physical parameters for this instability, while the values of other parameters were inferred under different assumptions discussed in their subsection 5.3. The observational values for these various parameters are listed in *Table 2* of Foullon et al. (2013). Among the most important parameters, they estimated a wavelength for the observed KH pattern of $\lambda = 18.5 \pm 0.5\ Mm$ and an instability growth rate of $\gamma_{KH} = 0.033 \pm 0.012\ s^{-1}$, which was driven by the velocity jump accross the shear layer of $680 \pm 92\ km.s^{-1}$. These numbers are in good agreement with the dispersion relationship of the KH instability (see § 4 below). The total magnetic field reported by Foullon et al. (2013) at the CME-pause is sufficiently strong to correspond to Alfven speeds comparable to the velocity jump accross the shear layer. However, as noted by these authors, the field is largely tangential to the interfase and normal to the KH flow. As a result, this large Alfven speed does not play any significant role in the development of the instability. In a series of compressible 2.5D MHD simulations Nykyri & Foullon (2013) managed to approximately reproduce the observed features of this KH event (see more details in §4).

Ofman & Thompson (2011) also reported observational evidence of the occurrence of the KH instability at the interface between a CME and the surrounding corona. Their

event took place on 2010 April 8, it was the first to be detected in EUV in the solar corona and was clearly observed by six out of the seven wave bands of AIA/SDO. The velocity jump accross the shear layer for this event was estimated in the range of $6 - 20\ km.s^{-1}$, while the wavelength of the observed KH pattern was $\lambda \simeq 7\ Mm$, based on the size of the initial ripples. From the dispersion relationship corresponding to an incompressible fluid with a discontinuous velocity jump, an instability growth rate of $\gamma_{KH} \simeq 0.005\ s^{-1}$ can be obtained. This value shows a reasonable agreement with the approximately 14 *min* over which the KH pattern was observed to grow and reach saturation (Ofman & Thompson 2011). The KH features, however, were observed to last for as long as 107 min. These observations were also compared with the results of compressible 2.5D MHD simulations, showing a good qualitative agreement during the nonlinear stage as well. Another KH event took place on 2011 February 24 in connection with a CME. Mostl et al. (2013) reported the quasi-periodic vortex structures observed by AIA/SDO and interpreted these observations with the aid of 2.5D MHD simulations. They find a reasonable agreement between the numerical results and the observations, assuming that the ejecta is about ten times denser than the surrounding ambient plasma.

2.2. Turbulent broadening

Spectroscopic studies of coronal spectral lines show quantitative evidence of the existence of spatially unresolved fluid motions through the nonthermal broadening effect on these lines. Early observations were performed by a number of instruments, such as the slit spectrograph aboard Skylab (Mariska 1992), the High Resolution Telescope Spectrograph rocket (Bartoe 1982), the Solar Ultraviolet Measurements of Emitted Radiation (SUMER) aboard the Solar and Heliospheric Observatory (Teriaca et al. 1999), or the various Solar Extreme Ultraviolet Research Telescope and Spectrograph flights between 1991 and 1997

(Coyner & Davila 2011).

More recently, Doschek et al. (2014) report nonthermal motions with velocities between 20 and 60 $km.s^{-1}$ obtained by EIS on *Hinode*, corresponding to regions at the loop tops and above the loop tops during several flares. EIS obtains images at the following two wavelength bands: $170 - 213$ $\AA$ and $250 - 290$ $\AA$. The angular resolution for the flare observations performed by Doschek et al. (2014) is about 2 $arcsec$. The line-of-sight motions responsible for these nonthermal broadenings correspond to plasma at temperatures in the range of $11 - 15$ MK, and they increase with the height above the flare loops.

These fluid motions have also been observed with EIS/Hinode in non-flaring active region loops (Doschek et al. 2008). These fluid motions are being carried out by plasma at temperatures of about $1.2 - 1.4$ MK with particle densities spanning the range of $5\ 10^8 - 10^{10}$ cm^{-3}. The rms values for the fluid velocities were in the range of $20 - 90$ $km.s^{-1}$. Outflow velocities in the range of $20 - 50$ $km.s^{-1}$ have also been detected through net blueshifts of the same spectral lines. The magnitude of the outflow velocities was found to be positively correlated with the rms velocity. Brooks and Warren (2011) performed a detailed study on active region AR 10978 using EIS/Hinode during a time span of five days in 2007 December. Persistent outflows were observed to take place at the edges of this active region, with an average speed of 22 $km.s^{-1}$ and average rms velocities of 43 $km.s^{-1}$. More recently, Tian et al. (2012) studied upflows in connection to dimming regions generated by CMEs, and reported velocities of up to 100 $km.s^{-1}$. It is speculated that these persistent outflows can be a significant source for the slow solar wind.

3. Magnetohydrodynamic description

The incompressible MHD equations for a fully ionized hydrogen plasma are the Navier-Stokes equation and the induction equation

$$\frac{\partial \boldsymbol{U}}{\partial t} = -\left(\boldsymbol{U}\cdot\boldsymbol{\nabla}\right)\boldsymbol{U} + v_A^2\left(\boldsymbol{\nabla}\times\boldsymbol{B}\right)\times\boldsymbol{B} - \boldsymbol{\nabla}P + \nu\nabla^2\boldsymbol{U} + \boldsymbol{F} \quad (1)$$

$$\frac{\partial \boldsymbol{B}}{\partial t} = \boldsymbol{\nabla}\times\left(\boldsymbol{U}\times\boldsymbol{B}\right) + \eta\nabla^2\boldsymbol{B}\ . \quad (2)$$

The velocity $\boldsymbol{U}$ is expressed in units of a characteristic speed U_0, the magnetic field $\boldsymbol{B}$ is in units of B_0, and we also assume a characteristic length scale L_0 and a spatially uniform particle density n_0. In general terms, the assumption of incompressibility is valid provided that the plasma velocity associated with the instabilities being considered (i.e. the fluctuating part of the velocity profile), remains significantly smaller than the speed of sound. Note that it is only the inhomogeneous part of the velocity field the one that should be much smaller than the speed of sound. This might be a good assumption for some KH events, while other KH events might require to include compressible effects. Notwithstanding, in the present paper we adopt incompressibility as a simplifying assumption. Because of quasi-neutrality, the electron and the proton particle densities are equal, i.e., $n_e = n_i = n_0$. The (dimensionless) Alfven speed is then $v_A = B_0/\sqrt{4\pi m_i n_0}U_0$, while η and ν are respectively the dimensionless magnetic diffusivity and kinematic viscosity. Note that for simplicity we assume isotropic expressions for both dissipative effects, even though in the presence of magnetic fields a tensor representation would be a more appropriate model (Braginskii 1965). These equations are complemented by the solenoidal conditions for both vector fields, i.e.,

$$\boldsymbol{\nabla}\cdot\boldsymbol{B} = 0 = \boldsymbol{\nabla}\cdot\boldsymbol{U}\ . \quad (3)$$

4. Kelvin-Helmholtz instability

Let us assume that the plasma is subjected to an externally applied shear flow given by

$$\boldsymbol{U}_0 = U_{0y}(x)\hat{\boldsymbol{y}}, \tag{4}$$

so that the total velocity field is now $\boldsymbol{U}_0 + \boldsymbol{u}$, where

$$U_{0y}(x) = U_0 \left[\tanh\left(\frac{x - \frac{\pi}{2}}{\Delta}\right) - \tanh\left(\frac{x - \frac{3\pi}{2}}{\Delta}\right) - 1 \right] , \tag{5}$$

The velocity profile given in Eqn. (5) simulates the encounter of largely uniform flows of intensities $+U_0\hat{\boldsymbol{y}}$ and $-U_0\hat{\boldsymbol{y}}$ through a parallel interface of thickness 2Δ. The numerical setup is sketched in Figure 1, where the jump provided by the hyperbolic tangent is duplicated to satisfy periodic boundary conditions throughout the numerical box. Also, we assume the presence of an external and uniform magnetic field $\boldsymbol{B}_0$ tangential to the interfase and almost perpendicular to the shear flow (see Fig. 1), so that the total magnetic field is $\boldsymbol{B}_0 + \boldsymbol{b}$. The assumption of a hyperbolic tangent velocity profile is often adopted (Drazin 1958; Chandrasekhar 1961; Miura 1992) as a way to model shear flows with a finite thickness. The velocity profile given in Eqn. (5) is an exact equilibrium of Eqs. (1)-(2) obtained through the application of the stationary external force $\boldsymbol{F}_0 = -\nu\nabla^2 U_{0y}(x)\hat{\boldsymbol{y}}$ (see also Gómez et al. (2014)), and therefore it is numerically implemented simply by the application of the volume force $\boldsymbol{F}_0$.

In the KH event that took place at one of the flanks of the 2010 November 3 CME, the fluid is observed to move along the contact discontinuity, albeit at very different speeds on either side. We choose to describe the development of the KH instability from a reference frame moving along the interfase at the average between these two speeds. In this reference frame, the flow will display a hyperbolic tangent type of profile, for which the parameter U_0 (see Eqn (5)) will be equal to one half of the relative velocity.

A shear flow such as the one given by Eqn. (5) is subjected to the well known Kelvin-Helmholtz instability, which is of a purely hydrodynamic nature, i.e. it occurs even in the absence of any magnetic field. Within the framework of MHD, the stability of a tangential velocity discontinuity (i.e. in the limit of $\Delta = 0$) was first studied by Chandrasekhar (1961). For the case of an external magnetic field aligned with the shear flow, the mode is stabilized by the magnetic field, unless the velocity jump exceeds twice the Alfvén speed. For the case at hand, we assume the parallel component of the external magnetic field to be sufficiently weak (i.e. $v_A^{\parallel} < 1$), since otherwise the instability pattern would not have been observed in AIA images. A stability analysis of a sheared MHD flow of finite thickness (i.e., $\Delta \neq 0$) in a compressible plasma has also been performed (Miura & Pritchett 1982), confirming the result of the purely hydrodynamic case. Compressibility has a stabilizing effect in the sense that the growth rate is reduced as the velocity jump approaches the speed of sound, and even stalls the instability when the Mach number becomes unity (Miura & Pritchett 1982). From *Table 2* of Foullon et al. (2013), we derive a shear flow amplitude $U_0 = 340 km.s^{-1}$, which remains below the speed of sound at both sides of the CME-pause. For the sake of simplicity, we neglect the effect of compressibility, which would bring an extra parameter to the problem: the Mach number. Yet another effect that might become relevant for the evolution of the KH instability, is the presence of a density contrast between both sides of the shear flow (Prialnik et al. 1986; Gonzalez & Gratton 1994; Wyper & Pontin 2013). However, for the particular event under consideration it is not expected to play a role, since the mass density at both sides of the CME-pause remains virtually the same (Foullon et al. 2013).

If we approximate the hyperbolic tangent profile given in Eqn. (5) by piecewise linear functions, the instability growth rate γ_{KH} arising from the linearized version of Eqs. (1)-(2)

is (for details, see Drazin & Reid (1981))

$$\left(\frac{\gamma_{KH}\Delta}{U_0}\right)^2 = \frac{1}{4}\left(e^{-4k_y\Delta} - (2k_y\Delta - 1)^2\right), \tag{6}$$

which attains its maximum at $\lambda_{max} \approx 15.7\ \Delta$ and $\gamma_{max} \approx 0.2U_0/\Delta$, as shown in Figure 2. More importantly, Figure 2 also shows that the KH instability only arises for large-scale modes, i.e. such that $k_y\Delta \leq 0.64$, corresponding to $\lambda \geq 9.82\Delta$.

We perform numerical integrations of Eqs. (1)-(2) subjected to the external force $\boldsymbol{F}_0 = -\nu\nabla^2 U_{0y}(x)\hat{\boldsymbol{y}}$ (where $U_{0y}(x)$ is given in Eqn. (5)) on the cubic box of linear size 2π sketched in Figure 1, assuming periodic boundary conditions in all three directions. The number of gridpoints is 256^3 and the dimensionless Alfven speed was set at $v_A^{\parallel} = 0.2$ in all our simulations, indicating that the component of the external magnetic field parallel to the flow (i.e. B_{0y}, see Fig. 1) is such that its associated Alfven velocity component remains smaller than the maximum velocity U_0 of the shear profile, and it is therefore unable to quench the instability. This is indeed the case of the 2010 November 3 KH event. Nykyri & Foullon (2013) performed a series of 2.5D MHD simulations seeking to match the time development of the KH pattern observed by AIA/SDO. Their numerical quest is consistent with slightly different magnetic field intensities at either side of the shear layer within the range of 8-11 G, forming small angles with the $\hat{z}$-direction (between 1° and 10°, see Fig. 1), which leads to values of $v_A^{\parallel}$ in the range of $v_A^{\parallel} \approx 0.04 - 0.31$.

In our simulations, we use a pseudospectral method to perform the spatial derivatives and a second order Runge-Kutta scheme for the time integration (see a detailed description of the code in Gómez et al. (2005)). For the viscosity and resistivity coefficients we chose $\nu = \eta = 2.10^{-3}$, which are small enough to produce energy dissipation only at very small scales, comparable to the Nyquist wavenumber. In particular, dissipative effects are certainly negligible for all wavenumbers becoming unstable due to KH (see Eqn. (6) and the text right below it). The values of all the dimensionless parameters

adopted for our simulations are summarized in Table 1. In all simulations, the pressure in Eqn. (1) is obtained self-consistently by taking the divergence of the equation, using the incompressibility condition, and solving at each time step the resulting Poisson equation for the pressure.

The evolution of the $\hat{\boldsymbol{z}}$-component of vorticity is shown in Figure 3 at three different times, displaying the characteristic pattern of the KH instability. The observed frame corresponds to the right half of the numerical box displayed in Figure 1, which covers the shear layer centered at $x_0 = 3\pi/2$, and has been rotated for better viewing. The observed pattern shows the presence of the largest Fourier mode in our numerical box, characterized by $k_y = 1$, whose growth rate according to Eqn. (6) is $\gamma_{KH}(k_y = 1) \simeq 0.87$. At the same time, the presence of harmonics is also apparent, judging by the smaller scale patterns showing up as the instability progresses. In fact, from Eqn. (6) (see also Figure 2) we can anticipate which ones would be the growing Fourier modes.

To estimate the instability growth rate, we use the component $u_x(x_0, y, z)$ evaluated at $x_0 = \pi/2, 3\pi/2$ (i.e., in the central part of the shear flows) as a proxy (see Figure 4). A Fourier analysis performed on $u_x(x_0, y, z)$ for any fixed value z, confirms that the exponentially growing modes belong to the interval $k_y = 1, \ldots, 6$; which is consistent with the theoretical prediction shown in Figure 2 for $\Delta = 0.1$. Since the KH pattern is a two-dimensional flow taking place at $z = constant$ planes, we take the maximum velocity of the profile $u_x(x_0, y, z)$ at any given value of z, and then average in the $\hat{\boldsymbol{z}}$-direction, i.e.

$$U_{x,max} = \int_0^{2\pi} \frac{dz}{2\pi} \max\left[u_x(x_0, y, z), 0 \leq y < 2\pi\right] \ . \tag{7}$$

In Figure 5 we show the maximum value of the $u_x(x_0, y, z)$ profile (averaged with respect to the $\hat{\boldsymbol{z}}$-direction) for both $x_0 = \pi/2$ and $x_0 = 3\pi/2$, although as expected the two curves are undistinguishable. The straight gray line corresponds to the theoretically predicted growth rate $\gamma_{KH} \simeq 0.87$ for the Fourier mode $k_y = 1$ (using Eqn. (6)), which

is the one observed in the time sequence shown in Fig. 3. The fact that our empirical determination of the growth rate so strongly resembles $\gamma_{KH}(k_y = 1)$ even though (as mentioned) the observed pattern is more complex that a single Fourier mode, arises as the combined result of the z-averaging and our choice of the maximum of the velocity profile, as defined in Eqn. (7). Note that even though the simulations include dissipative effects and the theoretical prediction does not, the coincidence between both curves during the linear regime of the instability is nonetheless remarkable. Considering that the attenuation effect of viscosity can be estimated by $\gamma \simeq \gamma_{KH} - \nu k_y^2$, we can easily verify that the dissipative correction is absolutely negligible for the evolution of the KH instability, as expected.

5. The turbulent corona

To generate a turbulent background in our simulations, we apply a stationary force to all modes within a thin spherical shell of radius $k_{turb} = 1/l_{turb}$ in Fourier space, consisting of a superposition of harmonic modes with random phases. The nonlinear interactions between these Fourier modes that are being externally driven with a force of intensity f_{turb}, will develop a stationary turbulent regime with its associated energy cascade involving all wavenumbers $k \geq k_{turb}$. To make sure that it is a small-scale turbulence, we chose l_{turb} to be much smaller than the wavelength observed for the KH pattern, and even somewhat smaller than the thickness Δ of the shear layer (i.e. $l_{turb} < \Delta$).

The pattern of vorticity obtained when only the turbulent forcing is applied (i.e. a simulation with no KH driving), is shown in Figure 6. The observed pattern corresponds to a turbulent regime which is statistically stationary, homogeneous and isotropic. Even though all spatial scales from l_{turb} down to the smallest scales available in the simulation participate in the dynamics and in the ensuing energy cascade, only those vortices of sizes comparable to l_{turb} can be identified, which is to be expected for a power law power

spectrum with a negative index such as Kolmogorov's. Therefore, these concentrations of vorticity can safely be associated to the energy-containing eddies of the turbulence. As mentioned in § 1, the expected effect of this small-scale turbulence on a larger scale flow, is an effective or enhanced diffusivity. In the case at hand, its effect on the instability growth rate is expected to be

$$\gamma(k) = \gamma_{KH}(k) - \nu_{turb} k^2 \ , \tag{8}$$

where $\gamma_{KH}(k)$ is given in Eqn. (6) and ν_{turb} is the aforementioned effective or turbulent viscosity. The effect of increasing turbulent viscosity on the instability growth rate is illustrated in Figure 7, showing that not only the growth rate is reduced but also the range of unstable wavenumbers.

We performed simulations applying both the large-scale force $\boldsymbol{F}_0$ to drive the KH instability and the small-scale force of intensity f_{turb} to drive the turbulent regime. In Figure 8 we show the resulting distribution of the vorticity component $\omega_z(x, y)$, which can be compared with the one shown in Figure 3 for the KH instability on a laminar background, and the one shown in Figure 6 for the purely turbulent run, with no KH pattern. We can qualitatively see that the role of turbulence is in fact an attenuation in the growth of the instability.

One of the observable consequences of this turbulent regime is the nonthermal broadening of coronal spectral lines caused by the turbulent motion of the fluid elements emitting these (optically thin) spectral lines. Once this turbulence reaches a Kolmogorov stationary regime, the rms value of the turbulent velocity u_{turb} is

$$E_{turb} = \frac{u_{turb}^2}{2} = \int_{1/l_{turb}} dk \ \epsilon^{2/3} \ k^{-5/3} \propto (\epsilon \ l_{turb})^{2/3} \ , \tag{9}$$

where E_{turb} is the (dimensionless) kinetic energy density of the turbulence and ϵ is its energy dissipation rate. Note that neither ϵ or E_{turb} are known a priori, since they arise as a result of the stationary regime attained by the turbulence. However, using heuristic arguments we

can find how these quantities scale with the input parameters of this turbulence: namely l_{turb} and f_{turb}. The fluid is energized by the work done per unit time by the external force of intensity f_{turb} at scale l_{turb}, energy then cascades down to smaller scales and it is dissipated by viscosity at the rate ϵ at dissipative scales. In a stationary regime, the power delivered by the external force should match the energy dissipation rate, i.e.

$$\epsilon \propto f_{turb}\ u_{turb}\ . \tag{10}$$

Equations (9)-(10) can be combined to obtain both u_{turb} and ϵ in terms of f_{turb} and l_{turb},

$$\epsilon \propto (f_{turb}^3\ l_{turb})^{1/2}\ , \tag{11}$$

$$u_{turb} \propto (f_{turb}\ l_{turb})^{1/2}\ . \tag{12}$$

On dimensional arguments, the turbulent viscosity introduced in Eqn. (8) has to be proportional to the turbulent velocity u_{turb} times the typical scale l_{turb}, i.e. $\nu_{turb} \propto u_{turb}\ l_{turb}$, which considering Eqn. (12)

$$\nu_{turb} = C(f_{turb}\ l_{turb}^3)^{1/2}\ . \tag{13}$$

6. Numerical results

To quantify the role of turbulence in the evolution of the KH instability, we performed a sequence of simulations for which the only parameter being changed is the turbulent forcing f_{turb}. As the parameter f_{turb} is gradually increased, the corresponding turbulent velocity u_{turb} (observationally perceived as nonthermal broadening of spectral lines) is also increased, which in turn raises the turbulent viscosity ν_{turb}. As a result, the instability growth rate (see Eqn. (8)) is expected to be reduced. To estimate the instability growth rate from our simulations, we follow the same procedure described in § 4, which amounts to follow the temporal evolution of the profile $u_x(y)$ for the gridpoints centered at the

shear layer. Note however, that now the velocity at each grid point can be split into a part corresponding to the large-scale KH evolution plus another part corresponding to the turbulence.

Because of the geometrical setup of our simulations, the large-scale part of the flow at each $z = constant$ plane is an exact replica of one another (KH is a two-dimensional flow) while the turbulent part is not, since it is a fully three-dimensional flow. The averaging procedure in the $\hat{\boldsymbol{z}}$-direction described in Eqn. (7) gets rid of the turbulent part of the flow, since the mean velocity of this turbulence is exactly zero. We can also compute the rms deviation of the velocity when averaging in the $\hat{\boldsymbol{z}}$-direction, which should exactly correspond to u_{turb}, since the KH part of the flow is identical for all $z = constant$ planes. Therefore, this statistical strategy allows us to obtain the main features of both the large-scale (i.e. the KH instability) and small-scale (the turbulence) components of this complex flow.

Figure 9 shows the main result of the present study, which is the value of $U_{x,max}$ (defined in Eqn. (7)) as a function of time in a lin-log plot, for runs corresponding to different turbulent intensities. The thick black lines corresponds to $U_{x,max}(t)$ for each simulation, the thin black lines indicate one standard deviation with respect to the average (i.e. $U_{x,max} \pm u_{turb}$), and the straight gray lines are the theoretical predictions for each case, as emerges from Eqn. (8). Note that the theoretical slopes (i.e. the gray lines in Figure 9) are not best fits to each of the simulations, but the result arising from Eqn. (8), which contains only one free parameter for the whole set of simulations, namely the constant C. This constant is the only dimensionless parameter that remains undetermined by the dimensional analysis described above. We find that the value of C that best fits all our simulations is $C \approx 18.8$.

7. Discussion

In the previous section, we presented results from numerical simulations showing the role of a background turbulence in reducing the growth rate of an ongoing KH instability. These numerical results are intended to simulate the KH instability being developed at the interface between some CMEs and the ambient corona, which have been recently reported in the literature. There is also mounting observational evidence about the turbulent nature of the solar corona, mostly related with spatially unresolved motions leading to measurable nonthermal broadenings in coronal spectral lines.

To numerically model this turbulent background, we made a number of simplifying assumptions. For instance, we assume the turbulent regime to be spatially homogeneous and isotropic and also stationary. We maintain this turbulent state throughout the whole simulation by applying a stationary stirring force of intensity f_{turb} at a well defined lengthscale l_{turb}. We deliberately chose this lengthscale to be much smaller than the wavelength of the KH unstable mode, since the AIA images reporting the KH pattern do not show any observable evidence of a turbulent background. Also, the rotation period of the energy-containing vortices is of the order of $\tau_{turb} \simeq l_{turb}/u_{turb}$, which remains shorter than the instability growth time for all the cases considered. The properties of this turbulent regime are therefore determined by only two input parameters: l_{turb} which is kept fixed throughout the whole study, and f_{turb} which is varied to give rise to cases with different turbulent velocities (u_{turb}) and effective viscosities (ν_{turb}).

We can use Eqs. (12)-(13) to express the effective viscosity ν_{turb} in terms of two measurable quantities such as u_{turb} and l_{turb}. A crude estimate of the dimensionless constant in Eqn. (12) leads to $u_{turb} \approx 0.22\ (f_{turb}\ l_{turb})^{1/2}$ and therefore

$$\nu_{turb} \approx 85.4\ u_{turb}\ l_{turb}\ . \tag{14}$$

If we refer for instance to the KH event occurred on 2010 November 3 and reported by Foullon et al. (2011), they estimate a velocity jump at the interface of $U_0 = 340\ km.s^{-1}$ and a wavelength for the KH pattern of $\lambda = 2\pi L_0 = 18.5\ Mm$ (corresponding to a length unit of $L_0 = 3\ Mm$ and $k_y = 1$ in our simulations). For $k_y = 1$, the dispersion relation reduces to $\gamma \approx 0.87 - \nu_{turb}$, as shown in Eqn. (8). The instability growth rate estimated by Foullon et al. (2013) for this event is $\gamma \approx 0.033\ s^{-1}$, which in our dimensionless units becomes $\gamma L_0/U_0 = 0.29 = 0.87 - \nu_{turb}$. From this expression we can estimate the value of ν_{turb} required to explain the growth rate observed for this particular KH event. More interestingly, using Eqn. (14) we can obtain a level of turbulent velocity of $u_{turb} \approx 47 km.s^{-1}$ (for the value of l_{turb} used in our simulations), which is well within the range reported by Doschek et al. (2014) from Hinode observations. It is important to recall that other effects besides turbulence might contribute to reduce the instability growth rate. Depending of the parameter values of the particular KH event being considered, the compressibility of the plasma or the strength of the magnetic field component along the shear flow might play a role.

Another consequence that we can derive from the present analysis is that, given the fact that the turbulence did not completely suppress the KH instability, we can in principle use Equations (8)-(14) to estimate an upper bound for l_{turb} for any observed value of u_{turb}. For the turbulent attenuation to be negligible (i.e. $\nu_{turb} \ll 0.87$) and assuming a turbulent velocity of 60 $km.s^{-1}$ (see Doschek et al. (2014)), we obtain for l_{turb} an upper bound of 170 km. In general,

$$l_{turb} \ll 170\ km(\frac{u_{turb}}{60\ km.s^{-1}})^{-1} \tag{15}$$

In summary, in order for the invoked turbulent state to produce nonthermal broadening of spectral lines of the order of u_{turb} and at the same time not to affect the observed KH event in any appreciable manner, the typical size l_{turb} of its energy-containing eddies should satisfy Eqn. (15).

8. Conclusions

The study presented in this paper was motivated by two relatively recent observational findings on the nature of the solar corona. One of them is the apparent development of the Kelvin-Helmholtz instability as some CMEs expand in the ambient corona, as shown by AIA/SDO images (Foullon et al. 2011, 2013; Ofman & Thompson 2011). The second one is that the coronal plasma seems to be in a turbulent state, as evidenced by the nonthermal broadening of coronal spectral lines measured from EIS/Hinode data (Doschek et al. 2008; Brooks and Warren 2011; Tian et al. 2012; Doschek et al. 2014).

Our main goal has been to study the feasibility for these two apparently dissimilar features to coexist. Namely, the large-scale laminar pattern observed for the KH instability, and the small-scale spatially unresolved turbulent motions leading to the observed nonthermal broadenings. We therefore performed three-dimensional simulations of the MHD equations, to study the evolution of the KH instability in the presence of a turbulent ambient background for different intensities of this turbulence.

Theoretically, the effect of a small-scale turbulence on a large-scale flow would be to produce an enhanced diffusivity which can be modeled by an effective or turbulent viscosity. The impact of this small-scale turbulence on an ongoing large-scale instability such as KH, would then be a reduction of its growth rate, as emerges from Eqn. (8). The degree of this reduction is controlled by the turbulent viscosity ν_{turb} which we obtained from a dimensional analysis to be $\nu_{turb} = C(f_{turb}\ l_{turb}^3)^{1/2}$ (see Eqn. (13)), leaving only the dimensionless constant C undetermined.

The comparison between the instability growth rates obtained from our simulations with the ones arising from Eqn. (8) esentially confirms this theoretical scenario, while providing an empirical determination for the dimensionless constant C, which amounts to $C \approx 18.8$. Perhaps more importantly, since $\nu_{turb} \propto u_{turb}\ l_{turb}$ and given the fact that the

instability has not been completely quenched by the turbulence (otherwise it would not have been observed), observational determinations of u_{turb} from nonthermal broadenings pose an upper limit to the correlation length of the turbulence l_{turb}. For observational values of $u_{turb} \approx 20 - 60\ km.s^{-1}$, the correlation length of turbulence is expected to be smaller than about $l_{turb} \approx 170 - 510\ km$, which is consistent with not having been spatially resolved by current coronal imaging spectrometers such as EIS aboard Hinode.

DG and EED acknowledge financial support from grant SP02H1701R from Lockheed-Martin to SAO. DG also acknowledges support from PICT grant 0454/2011 from ANPCyT to IAFE and PDM acknowledges support from PICTs 2011-1529 and 2011-1626 from ANPCyT to IFIBA (Argentina).

REFERENCES

Balbus, S.A., & Hawley, J.F. 1998, Rev. Mod. Phys., 70, 1

Bartoe, J.D. 1982, Adv. Space Res., 2, 185

Begelman, M.C., Blandford, R.D., & Rees, M.J. 1984, Rev. Mod. Phys., 56, 255

Bodo, G., Massaglia, S., Ferrari, A., & Trussoni, E. 1994, A&A, 283, 655

Braginskii, S.I. 1965, Rev. Plasma Phys., 1, 205

Brandt, J.C., & Mendis, D.A. 1979, "Solar System Plasma Physics", Eds. C.F. Kennel et al. (North Holland: Amsterdam), 2, 253

Brooks, D.H., & Warren, H.P. 2011, ApJ, 727, L13

Chandrasekhar, S. 1961, "Hydrodynamic and Hydromagnetic Stability", Oxford University Press: New York.

Coyner, A.J., & Davila, J.M. 2011, ApJ, 742, 115

Doschek, G.A., Warren, H.P., Mariska, J.T., Muglach, K., Culhane, J.L., Hara, H., & Watanabe, T. 2008, ApJ, 686, 1362

Doschek, G.A., McKenzie, D.E., & Warren, H.P. 2014, ApJ, 788, 26

Drazin, P.G. 1958, J. Fluid Mech., 4, 214

Drazin, P.G., & Reid, W.H. 1981, "Hydrodynamic Stability", Cambridge University Press: Cambridge.

Dwarkadas, V.V., & Balbus, S.A. 1996, ApJ, 467, 87

Ershkovich, A.I., Nusinov, A.A., & Chernikov, A.A. 1973, Soviet Astr., 16, 705

Fairfield, D.H., Otto, A., Mukai, T., Kokubun, S., Lepping, R.P., Steinberg, J.T., Lazarus, A.J., Yamamoto, T. 2000, J. Geophys. Res., 105, 21159

Ferrari, A., Trussoni, E., & Zaninetti, L. 1980, MNRAS, 193, 469

Foullon, C., Verwichte, E.,Nakariakov, V.M., Nykyri, K., & Farrugia, C.J. 2011, ApJ, 729, L8

Foullon, C., Verwichte, E., Nykyri, K., Aschwanden, M.J., & Hannah, I.G. 2013, ApJ, 767, 170

Fujimoto, M., & Teresawa, T. 1995, J. Geophys. Res., 100, 12025

Gonzalez, A.G., & Gratton, J. 1994, J. Plasma Phys., 52, 223

Gómez, D.O., Mininni, P.D., & Dmitruk, P. 2005, Phys. Scripta, T116, 123

Gómez, D.O., Bejarano, C., & Mininni, P.D. 2014, Phys. Rev. E, 89, 053105

Hasegawa, A. 1985, Adv. Phys., 34, 1

Helmholtz, H.L.F. 1868, Monthly Rep. Royal Prussian Acad. Phil. Berlin, 23, 215

Lau, Y.Y., & Liu, C.S. 1980, Phys. Fluids, 23, 939

Mariska, J.T. 1992, in *The Solar Transition Region* (Cambridge: Cambridge Univ. Press).

Masters, A., and 10 co-authors 2010, J. Geophys. Res., 115, A07225

Miura, A., & Pritchett, P.L. 1982, J. Geophys. Res., 87, 7431

Miura, A. 1992, J. Geophys. Res., 97, 10655

Mostl, U.V., Temmer, M., & Veronig, A.M. 2013, ApJ, 766, L12

Nykyri, K., & Otto, A. 2001, Geophys. Res. Lett., 28, 3565

Nykyri, K., & Foullon, C. 2013, Geophys. Res. Lett., 40, 4154

Ofman, L., & Thompson, B.J. 2011, ApJ, 734, L11

Parker, E.N. 1958, ApJ, 128, 6640

Poedts, S., Rogava, A.D., & Mahajan, S.M. 1998, ApJ, 505, 369

Prialnik, D., Eviatar, A., & Ershcovich, A.I. 1986, J. Plasma Phys., 35, 209

Sundberg, T., and 7 co-authors 2011, Planetary & Space Sci., 59, 2051

Teriaca, L., Doyle, J.G., Erdelyi, R., & Sarro, L.M. 1999, A& A, 352, L99

Tian, H., McIntosh, S.W., Xia, L., He, J., & Wang. X. 2012, ApJ, 748, 106

Thomson, W.(Lord Kelvin) 1871, Phil. Mag., 42, 362

Wyper, P.F., & Pontin, D.I. 2013, Phys. Plasmas, 20, 032117

This manuscript was prepared with the AAS LaTeX macros v5.2.

Table 1. Values of dimensionless parameters for the simulations: N is the linear size, U_0 is the velocity at each side of the shear layer, Δ is the thickness of the shear layer, $v_A^{\parallel}$ is the parallel component of the Alfvén speed, η is the magnetic diffusivity, ν is the kinematic viscosity, l_{turb} is the the length scale of the turbulence and f_{turb} is the strength of the turbulent forcing.

N	U_0	Δ	$v_A^{\parallel}$	η	ν	l_{turb}	f_{turb}
256	1	0.1	0.2	2.10^{-3}	2.10^{-3}	0.05	0, 2, 3, 4, 5, 10, 15

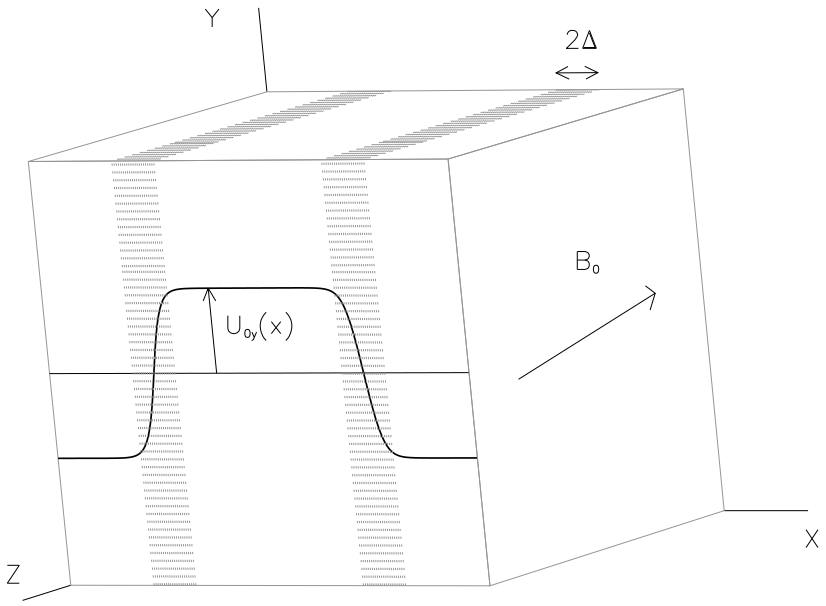

Fig. 1.— Numerical box displaying the imposed velocity profile $U_0(x)$ in the $\hat{y}$-direction and the external homogeneous magnetic field $\boldsymbol{B}_0$. The shaded patches correspond to regions with intense shear. Each axis ranges from 0 to 2π.

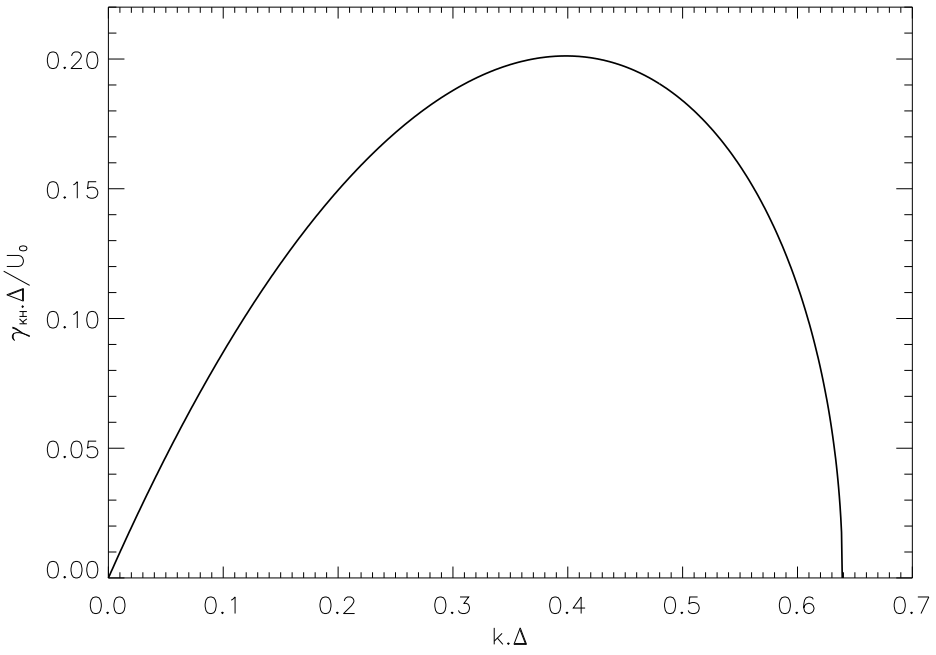

Fig. 2.— Growth rate for the Kelvin-Helmholtz instability of a shear layer with a velocity jump from $+U_0$ to $-U_0$ over a half-width Δ as a function of wavenumber.

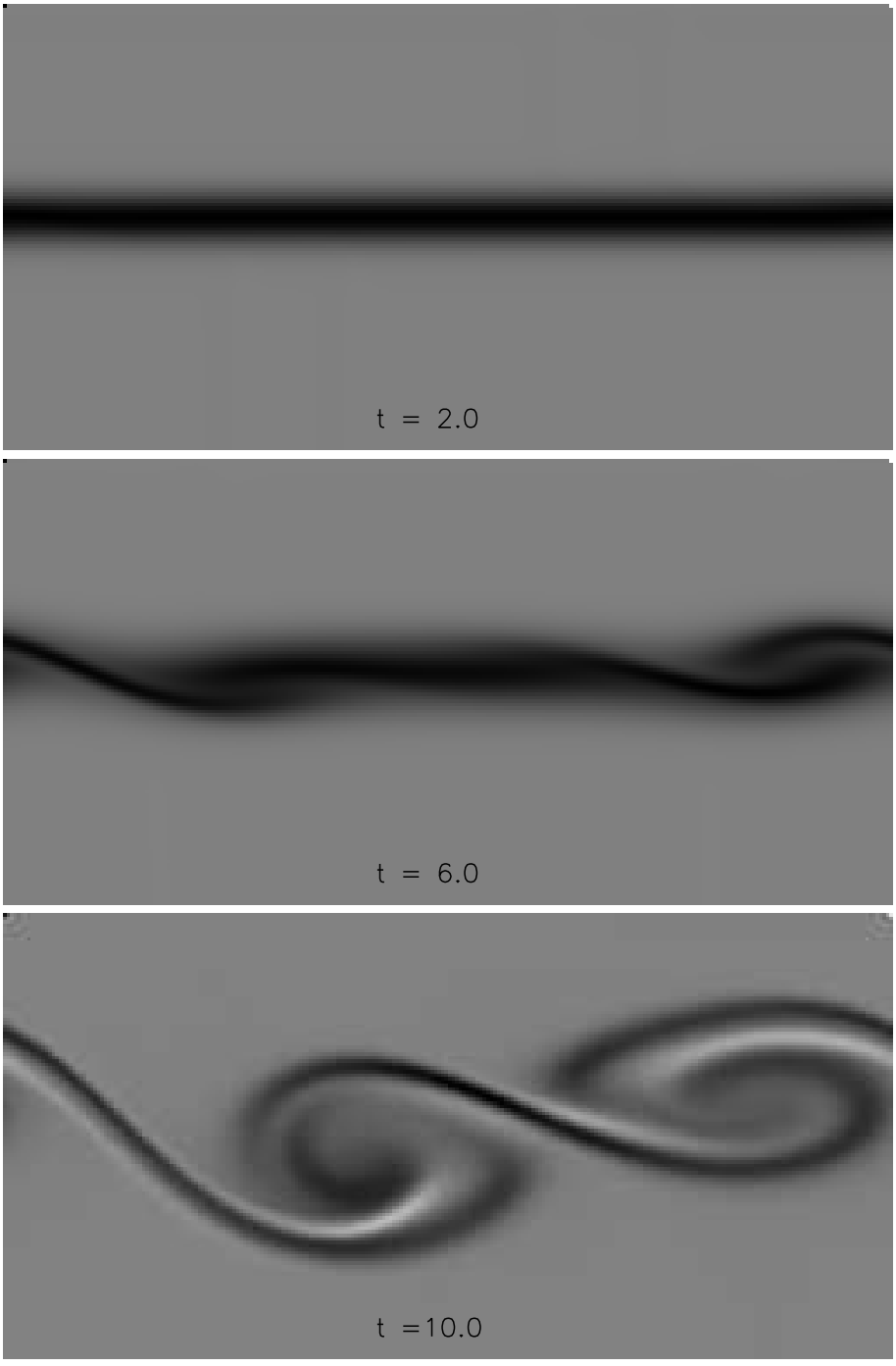

Fig. 3.— Time sequence (as labelled) of the vorticity component $\omega_z(x, y)$ at the plane $z = 2\pi$ for the right half of the numerical box shown in Fig. 1 (rotated 90°) for a purely shear-driven simulation. Gray corresponds to $\omega_z = 0$ while black (white) corresponds to negative (positive) concentrations of vorticity.

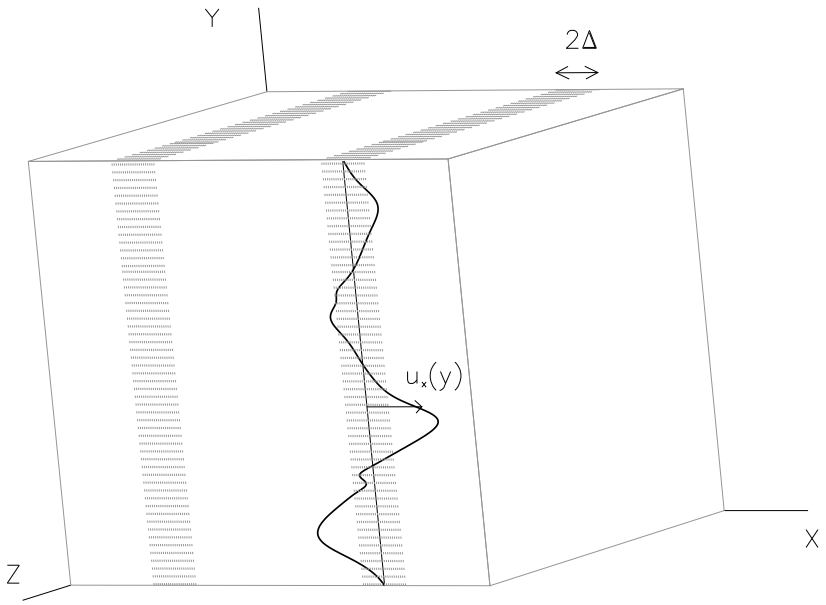

Fig. 4.— Numerical box (see also Fig. 1) displaying the velocity profile $u_x(y)$ for the slice located at the center of the shear layer. This velocity profile obtained for a sequence of times is used to estimate the instability growth rate.

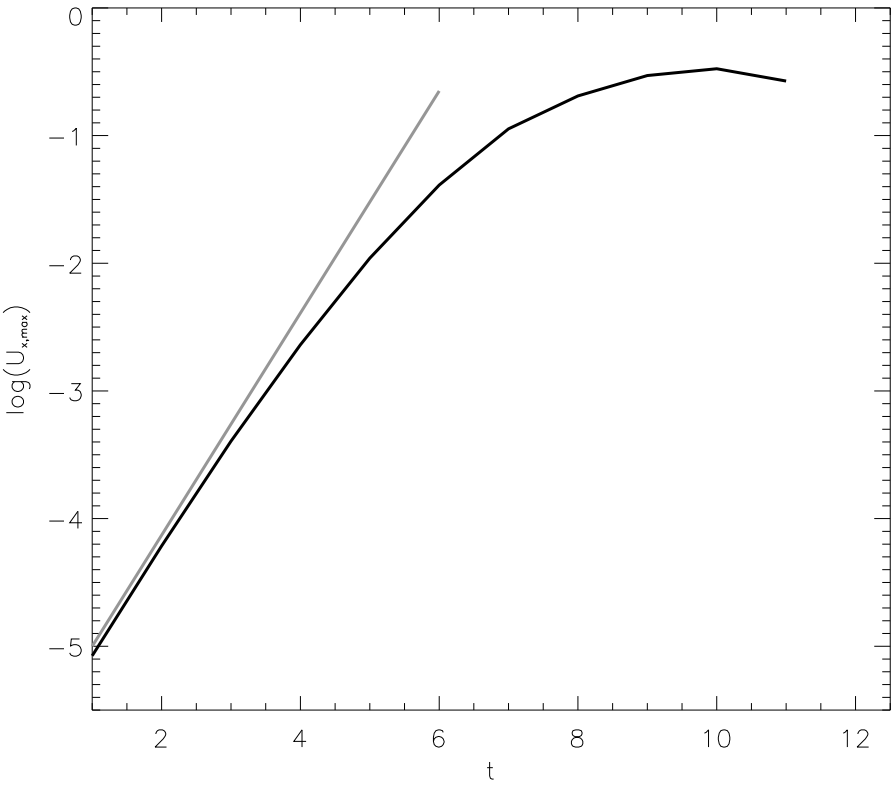

Fig. 5.— Maximum value of the profile $u_x(x_0, y)$ vs. time in a lin-log plot. The two black traces are indistinguishable from one another and correspond to $x_0 = \pi/2$ and $x_0 = 3\pi/2$. The straight gray line corresponds to the theoretical growth rate.

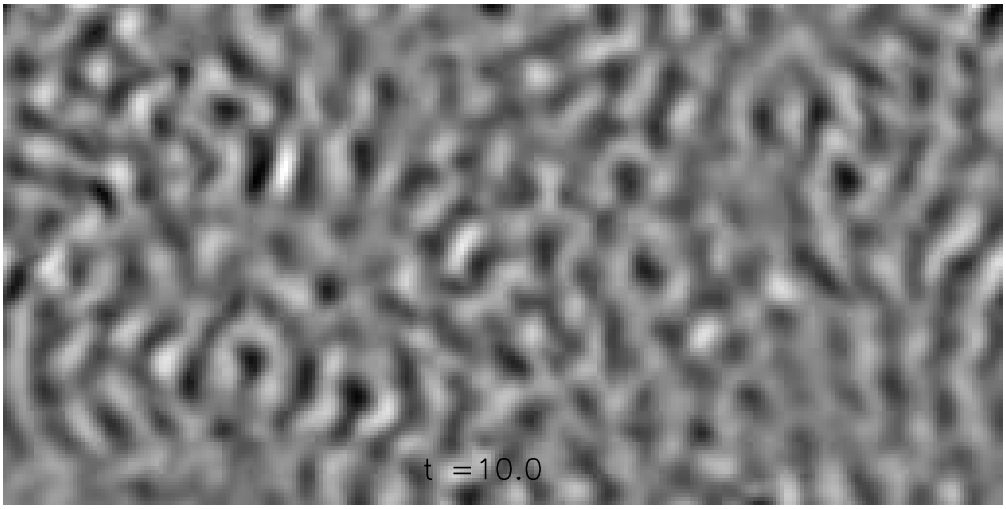

Fig. 6.— Vorticity component $\omega_z(x, y)$ at the plane $z = 2\pi$ for the right half of the numerical box shown in Fig. 1 (rotated 90°) for a purely turbulence-driven simulation at $t = 10$. Gray corresponds to $\omega_z = 0$ while black (white) corresponds to negative (positive) concentrations of vorticity.

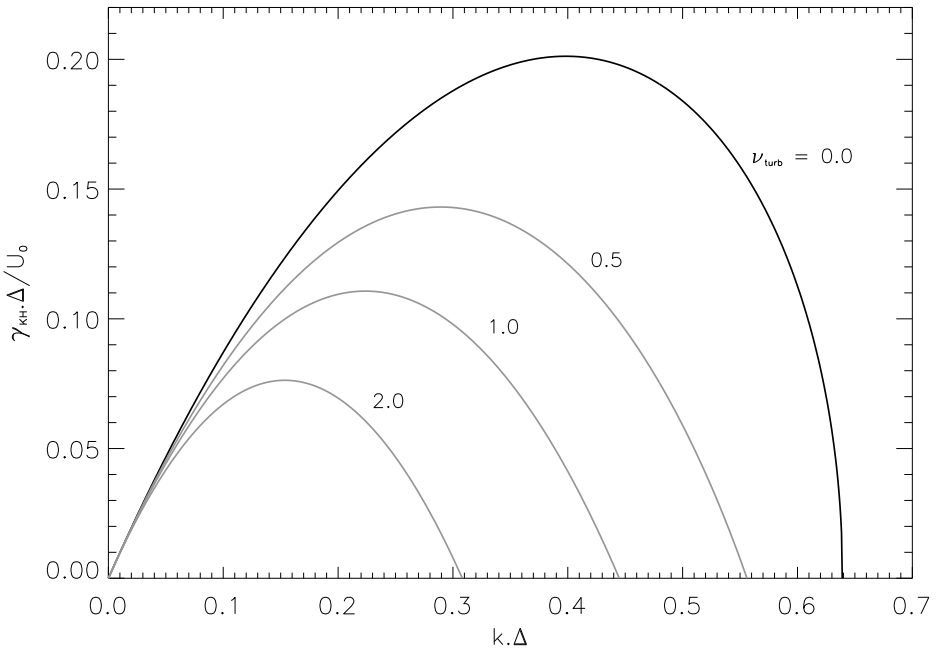

Fig. 7.— Instability growth rates vs. wavenumber. Black trace corresponds to Kelvin-Helmholtz in a non-turbulent medium, as shown in Fig. 2. Gray traces correspond to cases with different values of the turbulent viscosity ν_{turb} (labelled).

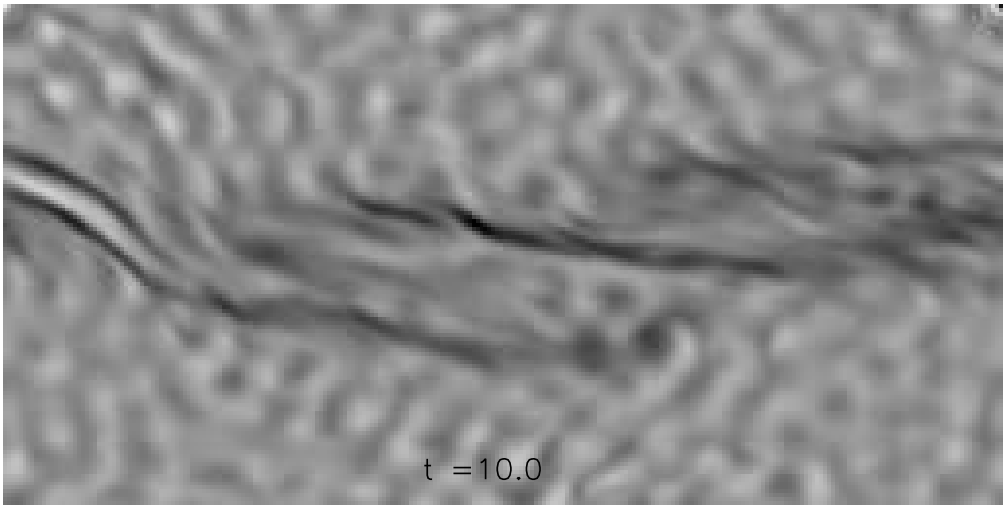

Fig. 8.— Vorticity component $\omega_z(x, y)$ at the plane $z = 2\pi$ for the right half of the numerical box shown in Fig. 1 (rotated 90°) for a shear and turbulence-driven simulation at $t = 10$. Gray corresponds to $\omega_z = 0$ while black (white) corresponds to negative (positive) concentrations of vorticity.

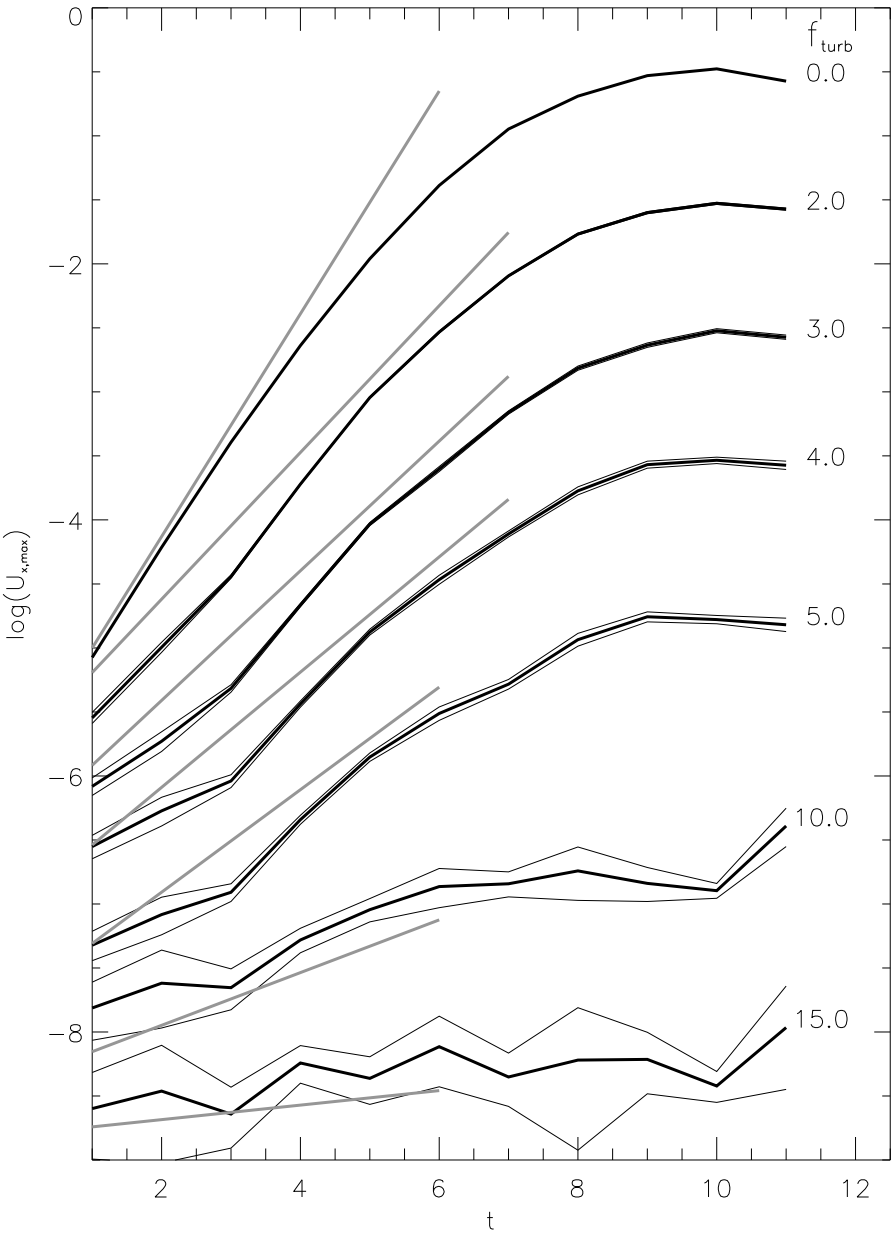

Fig. 9.— Maximum value of the profile $u_x(x_0, y)$ vs. time in a lin-log plot for runs of different turbulence intensities f_{turb} (labelled) and $x_0 = \pi/2$. Each thick black trace corresponds to the average in the $\hat{\boldsymbol{z}}$-direction, while the thin black traces (only noticeable for $f_{turb} = 4$ and larger) correspond to plus or minus the root-mean deviation of the average. The straight gray lines correspond to the theoretical growth rate shown in Eqn. (8).